ELSEVIER

Contents lists available at ScienceDirect

Materials & Design

journal homepage: www.elsevier.com/locate/matdes



Optimizing structural design on biodegradable magnesium alloy vascular stent for reducing strut thickness and raising radial strength



Yafei Li^a, Jianfeng Wang^{a,b,c}, Kun Sheng^a, Fulong Miao^a, Yan Wang^a, Yifan Zhang^a, Ruiqing Hou^{a,b}, Di Mei^{a,b}, Yufeng Sun^{a,b,c}, Yufeng Zheng^d, Shaokang Guan^{a,b,c,*}

- ^a School of Materials Science and Engineering, Zhengzhou University, Zhengzhou 450001, China
- ^b Henan Key Laboratory of Advanced Magnesium Alloys, Zhengzhou 450002, China
- ^cKey Laboratory of Advanced Materials Processing & Mold Ministry of Education, Zhengzhou 450002, China
- ^d School of Materials Science and Engineering, Peking University, Beijing 100871, China

HIGHLIGHTS

- A structural optimization strategy for thin-walled (100 μm) magnesium alloy vascular stents was proposed.
- The radial strength of the optimized thin-walled stent (100 μ m) can match the effect of the original thick-walled stent (150 μ m).
- The foreshortening and coverage of the optimized thin-walled stent are significantly reduced, the vascular damage is smaller, which is expected to have better biocompatibility.

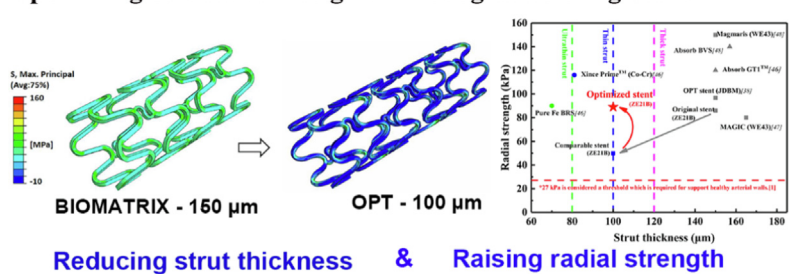
ARTICLE INFO

Article history:
Received 2 April 2022
Revised 29 May 2022
Accepted 10 June 2022
Available online 14 June 2022

Keywords: Structural design Finite element analysis Biodegradable magnesium alloy stents Radial strength

G R A P H I C A L A B S T R A C T

Optimizing Structural Design on Biodegradable Mg Stent



ABSTRACT

Thinner biodegradable magnesium alloy stents (BMgSs) afford faster endothelialisation to delay degradation and better clinical performance. However, compared with traditional non-degradable stents, thin-walled BMgS structures are prone to challenges, such as insufficient support capacity and fracture, during immediate expansion due to low elastic modulus and ultimate elongation. In this study, a thin-walled BMgS structure was optimised. A ZE21B alloy with large breaking elongation and excellent mechanical properties served as the basis of our BMgS. Using finite element analysis, the support ring structure of a typical stent BioMatrix was optimised using response surface models, and an optimised configuration of a thin-walled BMgS was obtained. The optimised thin-walled stent (100-µm thick) had a radial strength comparable to that of the original thick-walled stent (150-µm thick); and the maximum principal strain is significantly decreased (0.207 vs 0.283). The balloon dilation and radial strength tests were validated. Experiments showed that the optimised stent had sufficient deformation stability during the crimping and expansion processes, and there was no strut fracture. Furthermore, the maximum principal stress area of the stent and the damage to the stenotic artery were significantly improved after optimisation.

© 2022 The Authors. Published by Elsevier Ltd. This is an open access article under the CC BY-NC-ND license (http://creativecommons.org/licenses/by-nc-nd/4.0/).

^{*} Corresponding author at: School of Materials Science and Engineering, Zhengzhou University, Zhengzhou 450001, China. *E-mail address:* skguan@zzu.edu.cn (S. Guan).

1. Introduction

The use of permanent metallic drug-eluting stents (DESs) can cause long-term complications, such as stent thrombosis and chronic inflammation [1–4]. These shortcomings have prompted the development of bioresorbable scaffolds (BRSs), which free blood vessels from permanently implanted metal stents, thus preventing the late adverse effects associated with DESs [5–8].

BRSs can be classified into biodegradable polymeric and metal stents, which include biodegradable magnesium alloy stents (BMgS) [9-12]. For biodegradable polymeric stents, the clinical use of the ABSORB bioresorbable vascular scaffold (BVSs) was approved by the Food and Drug Administration (FDA) in 2015 [13]. However, the Absorb BVS was withdrawn from the market in 2017 by FDA because of thick struts (157 µm) and strut malapposition. Other degradable polymer stents available on the market also have the problem of thick struts, such as Xinsorb scaffolds (150-160 µm, Huaan Biotch) and NeoVas scaffolds (180 µm, Lepu Medical Technology) [14]. The BMgS has developed rapidly with higher biocompatibility and improved mechanical properties compared with biodegradable polymeric stents. However, due to its rapid and uneven degradation, the BMgS still requires high thickness to maintain the early radial support, yielding slower endothelialization and worse biocompatibility: in turn. a thinner biodegradable magnesium alloy stent (BMgS) results in faster endothelialization to delay degradation and better clinical performances [14,15]. Previous studies have indicated that stent thickness exceeding 100 µm considerably increases the risk of late restenosis [15-18].

Reasonable structural design is one of the significant factors for vascular stents to achieve the expected performance [19–27]. The optimization of stent design by finite element analysis (FEA) has been proved to be a cost-effective method to improve the performance of traditional metal stents; thus, FEA has become a fast, economical and effective research tool [28-32]. For example, DREAMS-2G has a higher strut thickness (\sim 150 μ m) to increase radial strength and fewer connecting links to achieve better-bending flexibility, secure mechanical integrity of the stent for at least 6 months before degradation causes a stent fragmentation [33–35]. Sriram et al. [31] optimized several competing objectives through the design of 316 L stainless steel stent structure in order to minimize the risk of arterial injury and maintain the stability of stent. Li et al. [36] optimized the expansion performance of the polymer stent by using the kriging model, and optimized the radial recoiling and foreshortening. Chen et al. [37] reduced the equivalent plastic strain of expand (PEEQ_{ex-} pand) during the deformation of BMgS by shape optimization strategy, this optimization strategy can make the stent deformation more uniform during the crimping and expansion process, and can effectively slow down stress corrosion; however, the stent remained extremely thick (150-160 µm). For the thin-walled structural designs of BMgSs, improving the radial strength and reducing the residual stress are challenging [38].

In this study, the thickness of a 150- μ m-thick stent was reduced to 100 μ m. The support structure was parameterised and set to four parameters: the length (L) and width (W1) of the ring, and the major axis (R) and width (W2) of the corner. First, training sample points are generated using Optimal Latin Hypercube Sampling (OLHS) during design optimisation. Then, the response surface method (RSM) proxy model is constructed to establish the relationship between the parameters and four optimisation objectives, including the PEEQ_{expand}, radial strength, radial recoiling and surface coverage. Finally, the optimised configuration of thin-walled (100- μ m) BMgS is obtained and compared with the initial stent (150- μ m) configuration, which includes the maximum principal strain, radial strength and effects on vascular damage.

2. Materials and methods

2.1. Material properties

A ZE21B alloy was supplied by Henan Key Laboratory of Advanced Magnesium Alloys, China [39–41]. The density of extruded ZE21B is 1780 Kg/m³, Poisson's ratio is 0.31, Young's modulus is 42.0 GPa. Uniaxial stretching is used to measure the mechanical properties of the ZE21B mini-tube. All simulations used the mechanical properties of the ZE21B alloy (Table 1) [42].

2.2. Stent and finite element modelling

A BioMatrix stent shape was investigated in this study. The geometries of the stent considered here are described in [29]. The stent was developed using a typical geometrical sin-wave crown and the design of two s-shaped links to achieve betterbending flexibility (Fig. 1). Fig. 1 shows the planar view of the BioMatrix stent structure and a unit cell with four changeable parameters. The width (W_{strut}) and thickness (T_{strut}) of the baseline strut were 0.14 mm and 0.15 mm, respectively. The internal diameter and L of the stent were 2.00 and 0.80 mm, respectively. The width of the connecting links is set to a fixed value of 0.10 mm.

Fig. 2 shows a three-dimensional (3D) finite element model of the stent crimping and expansion processes in the artery. The Poisson's ratio of the balloon is 0.3 and the Young's modulus is 1455 MPa. The stent was pressed to an outer diameter of 1.50 mm using a 12.00-mm-long and 2.50-mm-diameter press grip shell (Fig. 2a and b) 1.50 mm outside diameter with a 12.00-mm long and 2.50 mm diameter press grip shell (Fig. 2a and b) and assembled to the blood vessel and balloon model (Fig. 2c). The balloon's diameter was expanded from 0.90 to 2.90 mm by radial displacement of the balloon (Fig. 2d). The balloon was removed, and the expanded stent was rebound freely. The final states of the stent and blood vessels are shown in Fig. 2e.

Radial strength was defined as the intercept of the radial load curve with a parallel line of the cycle loading line starting from 90% of the original size (zero-compression diameter) at the xaxis, as shown in our previous report [41]. The artery is modelled as a cylinder. The wall thickness and inner diameter of the blood vessel are 0.58 mm and 3.00 mm, respectively. The density of blood vessel is 1.12×10^{-3} g/mm³. Holzapfel et al [18] proposed a constitutive model for each of the three layers—intima, media and the adventitia. This study selected a 6th order reduced polynomial to model a blood vessel, and the coefficients for media are used in this study as the artery is assumed to be composed of a single layer [42]. In the model, the stent and artery were modelled using C3D8R. The grid is too rough to reach the accuracy we want. Instead, if the mesh is too fine, it is easy to cause excessive calculations. Therefore, the average feature length of the stent mesh is set to 0.02 to ensure convergence [29]. The balloon was modelled as M3D4R. The stent was meshed with 120,000 to 190,000 C3D8R elements because of the parameterisation variation of each simulation. The interaction between components was simulated

Table 1The ZE21B alloy's true stress-strain data

Stress (MPa)	Plastic strain				
185.00	0				
200.32	0.0488				
269.45	0.0953				
311.16	0.1398				
365.16	0.1823				

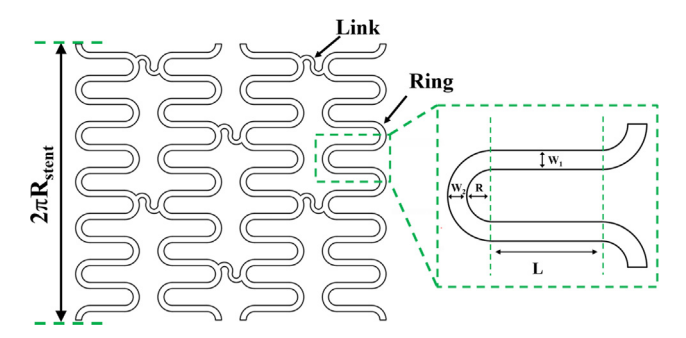


Fig. 1. Planar view of the BioMatrix stent structure and a unit cell showing four changeable parameters.

using a general contact (explicit) algorithm, the tangential friction coefficient was set to 0.2 and the normal contact was hard [43]. ABAQUS/Explicit solution (version 6.14-1) was used for FEA and calculations.

2.3. Sampling strategy and optimisation algorithm

Although the traditional Monte Carlo method is simple, it cannot guarantee uniform space-filling. Thus, the OLHS sampling strategy is an effective alternative for establishing the most accurate alternative model from as few sample points as possible [44]. The polynomial RSM is a commonly used proxy model method that uses polynomial as a fitting function. The RSM method is suitable for solving low-dimensional problems with high efficiency, and it can give explicit expressions directly [45]. Therefore, this study selects RSM model for optimization design.

2.4. Optimisation strategy and process

Increasing radial strength and reducing stress corrosion is the key to preventing the early failure of BMgSs. Thus, this study mainly balances the relationship between equivalent plastic strain and radial support strength. The optimal solution was searched using the non-dominated sorting genetic algorithm II. Fig. 3 depicts the flowchart used in this study.

The optimisation design limits stent coverage to less than 20%. The structure is parameterised and set as four parameters: the length (L) and width (W1) of the support ring, and the major axis (R) and width (W2) of the corner (Fig. 1). The parameter range can be written as follows:

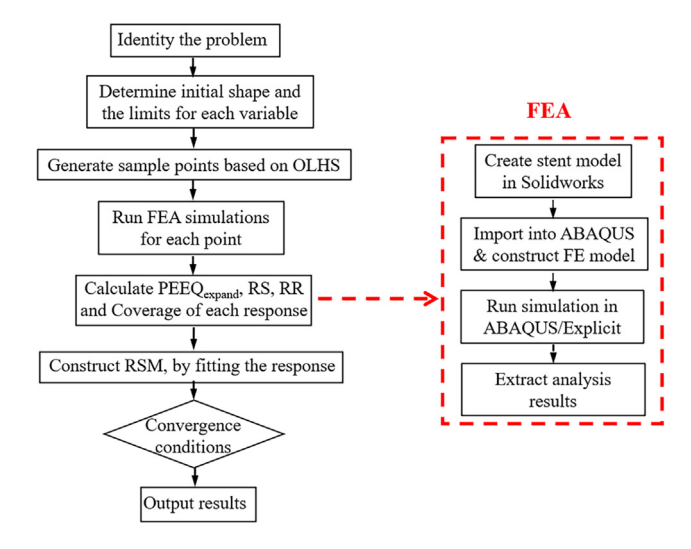


Fig. 3. The flowchart describing the optimization methodology process.

$$0 \text{ mm} < L < 0.250 \text{ mm}$$
 (1)

$$0.125 \text{ mm} \le W1 \le 0.175 \text{ mm}$$
 (2)

$$0.250 \text{ mm} \le R \le 0.500 \text{ mm}$$
 (3)

$$0.090 \text{ mm} < W2 < 0.290 \text{ mm}$$
 (4)

2.5. In vitro mechanical experiments

The ZE21B micro-tubes used in this research were supplied by Henan Key Laboratory of Advanced Magnesium Alloys, China [39–42]. The stents were laser-cut (Starcut Tube SL, Germany) directly from the micro-tubes, followed by electrochemical polishing and ultrasonic cleaning. The electrolytic polishing solution used in the experiment is perchloric acid ethanol solution, which is cooled with dry ice during use. Larger polishing margin and longer polishing time were set in thicker wall microtubules to reduce the thickness of the stent to $100~\mu m$. A Model CX stent crimping machine (Blockwise, American) was used to crimp, and a balloon catheter with an inflator device was used to expand the stents. A pressure of 0–6 atm was applied to the balloon, and an optical microscope was used to record the stent morphological changes during the balloon expansion and deflation. To investigate

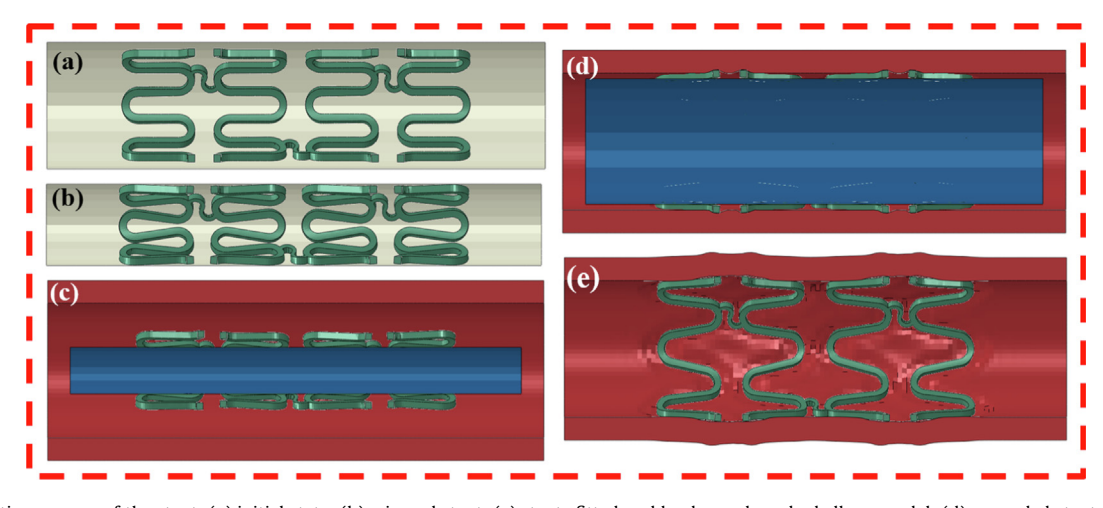


Fig. 2. Deformation process of the stent: (a) initial state; (b) crimped stent; (c) stents fitted on blood vessels and a balloon model; (d) expanded stent and (e) final state.

the compression resistance performance, the expanded ZE21B stent was tested using Model TTR2 Radial Force Tester (Blockwise, American) based on the ASTM F3067-14 standard. The foreshortening, radial recoiling (RR) and dog-boning rates were calculated using the following equations.

$$Radial\ recoiling(RR) = \frac{R_{loading} - R_{unloading}}{R_{loading}} \times 100\% \tag{5}$$

$$Foreshortening(FS) = \frac{\textit{L}_0 - \textit{L}_{unloading}}{\textit{L}_0} \times 100\% \tag{6}$$

Dog boning rate =
$$\frac{D_{inflating}^{distal} - D_{inflating}^{central}}{D_{inflating}^{distal}} \times 100\%$$
 (7)

$$Coverage = \frac{S_{stent}}{S_0} * 100\%$$
 (8)

where $R_{loading}$ and $R_{unloading}$ are the radial diameters of the stent's full expansion and unloading, respectively. L_0 and $L_{unloading}$ are the initial and unloaded lengths of the stent, respectively. The $D_{inflating}^{central}$ and $D_{inflating}^{distal}$ are the maximum values of the central diameter and distal diameter of the whole stent, respectively. The S_{stent} is the outer surface area of the stent, S_0 is a cylindrical area of diameter and length as the stent.

2.6. Statistics and date analysis

Statistical analysis was performed with Origin 2017 software package (OriginLab Inc. Northampton. USA). Statistical significance of difference between groups was assessed by one-way analysis of variance (ANOVA) followed by post hoc Tukey's multiple comparison test. *P* values less than 0.05 were considered statistically significant.

Table 2 Result matrix for the initial sampling and corresponding target values

Design	Geometry s	structure size			PEEQexpand	Radial strength (kPa)	Radial recoiling	Coverage (%)	
	L (mm) R (mm)		W1 (mm) W2 (mm)		*				
DOE-1	0.0000	0.2789	0.1731	0.1516	0.4328	141.81	0.0367	13.69	
DOE-2	0.0399	0.4711	0.1693	0.2453	0.1564	89.25	0.0670	20.04	
DOE-3	0.1399	0.3137	0.1519	0.2597	0.2057	89.25	0.0570	20.21	
DOE-4	0.2101	0.3269	0.1404	0.0938	0.1524	99.91	0.0664	12.31	
DOE-5	0.1601	0.3078	0.1423	0.1947	0.1206	103.88	0.0592	16.40	
DOE-6	0.2304	0.4423	0.1615	0.1803	0.0855	82.95	0.0664	20.19	
DOE-7	0.0601	0.4231	0.1558	0.2813	0.1358	85.71	0.0522	22.39	
DOE-8	0.2203	0.5000	0.1500	0.2163	0.0624	75.59	0.0875	18.40	
DOE-9	0.0899	0.3558	0.1289	0.1659	0.1114	97.92	0.0613	16.32	
DOE-10	0.1899	0.4808	0.1328	0.1875	0.0637	72.32	0.0814	16.67	
DOE-11	0.0101	0.2693	0.1519	0.1225	0.2058	122.88	0.0496	13.52	
DOE-12	0.0804	0.3461	0.1635	0.1009	0.1658	115.76	0.0537	17.16	
DOE-13	0.2500	0.2885	0.1711	0.2525	0.1639	101.56	0.0617	21.34	
DOE-14	0.1304	0.4135	0.1250	0.2234	0.1093	77.60	0.0744	17.04	
DOE-15	0.2405	0.2981	0.1269	0.2381	0.1900	73.98	0.0592	17.97	
DOE-16	0.1703	0.2596	0.1346	0.1444	0.1119	105.09	0.0583	11.77	
DOE-17	0.0203	0.3750	0.1673	0.2306	0.1698	103.04	0.0491	19.47	
DOE-18	0.2000	0.3846	0.1481	0.1369	0.0984	89.49	0.0670	16.44	
DOE-19	0.1101	0.4328	0.1308	0.1153	0.0817	90.32	0.0701	14.50	
DOE-20	0.1000	0.3654	0.1365	0.2741	0.2319	82.45	0.0647	18.74	
DOE-21	0.1500	0.3365	0.1596	0.1731	0.1354	105.79	0.0562	18.17	
DOE-22	0.0703	0.4039	0.1443	0.2091	0.1027	91.31	0.0651	17.84	
DOE-23	0.0500	0.4904	0.1461	0.1297	0.0989	90.75	0.0676	15.39	
DOE-24	0.1203	0.4519	0.1654	0.1081	0.1813	85.29	0.0609	16.96	
DOE-25	0.0297	0.4615	0.1385	0.2669	0.1775	88.90	0.0649	17.09	
DOE-26	0.1804	0.2500	0.1578	0.1947	0.1567	120.02	0.0467	18.83	

3. Results

3.1. Sample points results

After FEA, the response results of sample points were calculated from the FEA output database, and the results are shown in Table.

2. The OLHS was adopted to generate these 26 sample points.

3.2. Optimisation process and FEA results

Fig. 4 shows the structural change, and the maximum principal stress distribution of the expanded original 150 μ m thickness Bio-Matrix stent (BIOMATRIX-150- μ m stent) and the expanded 100 μ m thickness-optimised stents (OPT-100- μ m stent).

Fig. 5 shows the FEA results of the BIOMATRIX-150-μm and OPT-100-μm stents. For the BIOMATRIX-150-μm stent, a maximum principal strain of 0.056 was found after crimping and recoiling (Fig. 5a). A radial recoil of 6.2% was discovered after the balloon was dilated and recoiled (Fig. 5b). Furthermore, a maximum principal strain of 0.283 was discovered after the balloon was dilated and recoiled. When the OPT-100-μm stent was crimped and recoiled, the maximum principal strain was 0.052 (Fig. 5c). A radial recoil of 5.3% was discovered after the balloon was dilated and recoiled (Fig. 5d). When the balloon attained its maximum value and recoiled, the maximum principal strain after dilation was 0.207, which is decreased by 26.9% [41].

3.3. Balloon expansion and dog-boning effect

The difference between the BIOMATRIX-150-μm and OPT-100 μm stents were verified by balloon dilation (including fore-shortening and RR) and the dog-boning effect (Fig. 6). Both the BIOMATRIX-150-μm and OPT-100-μm stents did not undergo circumferential rotation during the deformation process and possessed sufficient deformation stability. The dog-boning effect of the BIOMATRIX-150-μm and OPT-100-μm stents was most obvious at 1.5 and 2.0 atm, respectively, but disappeared at 3.0 atm. All the stents could be completely expanded while keeping their

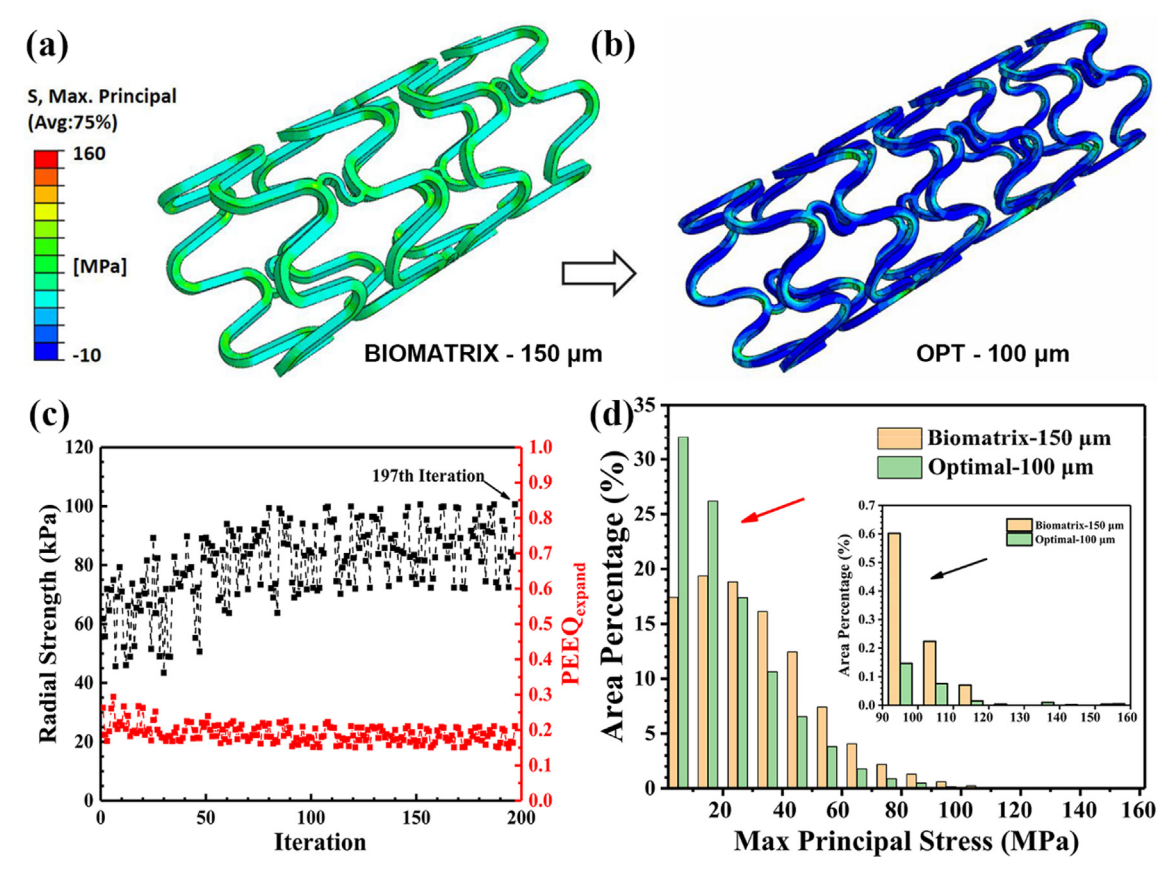


Fig. 4. The maximum principal stress distribution of the (a) BIOMATRIX-150 μ m and (b) OPT-100 μ m stents after balloon inflation and recoil. (c) Optimisation history showing the relationship between the radial strength and PEEQ_{expand}. (d) The histograms of the max principal stress of the BIOMATRIX-150 μ m and OPT-100 μ m stents. The red and black arrows indicated the low-stress and high-stress areas, respectively.

shapes intact. The OPT-100- μ m stent had less RR (6.2% ± 0.5% vs 6.5% ± 0.7%), dog-boning (21.1% ± 0.9% vs 25.9% ± 2.0%) and similar foreshortening (3.6% ± 0.9% vs 4.7% ± 1.3%) than the BIOMATRIX-150- μ m stent. Both the foreshortening and RR of the OPT-100- μ m stent were \leq 15.0%, matching the standard of ISO 25539–2:2008.

3.4. Radial strength

The radial strengths of the stents are shown in Fig. 7. When the structure was the same as the BIOMATRIX-150- μm stent, the thickness of the comparative stent was reduced by 50 μm , and the radial strength was reduced by 41.9% (50 \pm 6 kPa vs 86 \pm 6 kPa). With the same thickness, the radial strength of the OPT-100- μm stent was increased to 89 \pm 4 kPa through structural optimisation. Although the simulated radial strength of the OPT-100- μm stent was lower than that of the BIOMATRIX-150- μm stent, the experimental measurement results are slightly higher than those before optimisation.

3.5. Damage to blood vessels

Fig. 8 shows the von Mises stress distribution of blood vessels after BIOMATRIX-150- μ m, BIOMATRIX-100- μ m and OPT-100- μ m stent implantation. The results show that the BIOMATRIX-150- μ m stent causes significant damage to blood vessels, with a maximum value of 128 kPa (Fig. 8a and b). However, for the BIOMATRIX-100- μ m stent, the value is approximately 30 kPa, which is much smaller than that of the BIOMATRIX-150- μ m stent (Fig. 8a). Furthermore, for stents with the same thickness, the opti-

mised OPT-100- μ m stent is 18 kPa (compared with BIOMATRIX-100- μ m stent decreased by 40.6%). The maximum principal stresses of the OPT-100- μ m stent increased significantly (67.5% vs 55.6%) in the low stress area (\leq 2.5 kPa), and the stress accounted for a relatively small proportion (23.5% vs 36.0%) in the stress area of 2.5–5 kPa (Fig. 8c).

4. Discussion

4.1. Relationship between optimisation components and design parameters

This study shows the influence of four stent optimisation parameters for BIOMATIRIX stents, including PEEQexpand, radial strength, RR and surface coverage (Fig. 9). The results show that W1 is crucial to the performance of the stent (Fig. 9a, b, c and d). PEEQ_{expand}, radial strength, RR and coverage were 62%, 56%, 59% and 61%, respectively (Fig. 9e, f, g and h). For the PEEQexpand, it is mainly related to the width of the support ring (W1, 62%), followed by the width of the arc (W2, 13%), arc major axis (R, 13%) and ring length (L, 12%). The difference is that the proportion of the arc major axis (R) was increased to 19% for the radial strength, whereas the influence of the arc width and major axis was relatively small (13% vs 12%). For RR, the proportion of the arc major axis was increased to 22%, whereas W2 decreased to 6%, indicating that adjusting the arc major axis of the stent can affect its RR more than the arc width. Finally, surface coverage is a key factor affecting stent endothelialisation. As expected, it is primarily related to the W1 (61%) and W2 (24%), whereas the influence of the arc major axis and ring length is relatively small (8% vs 7%).

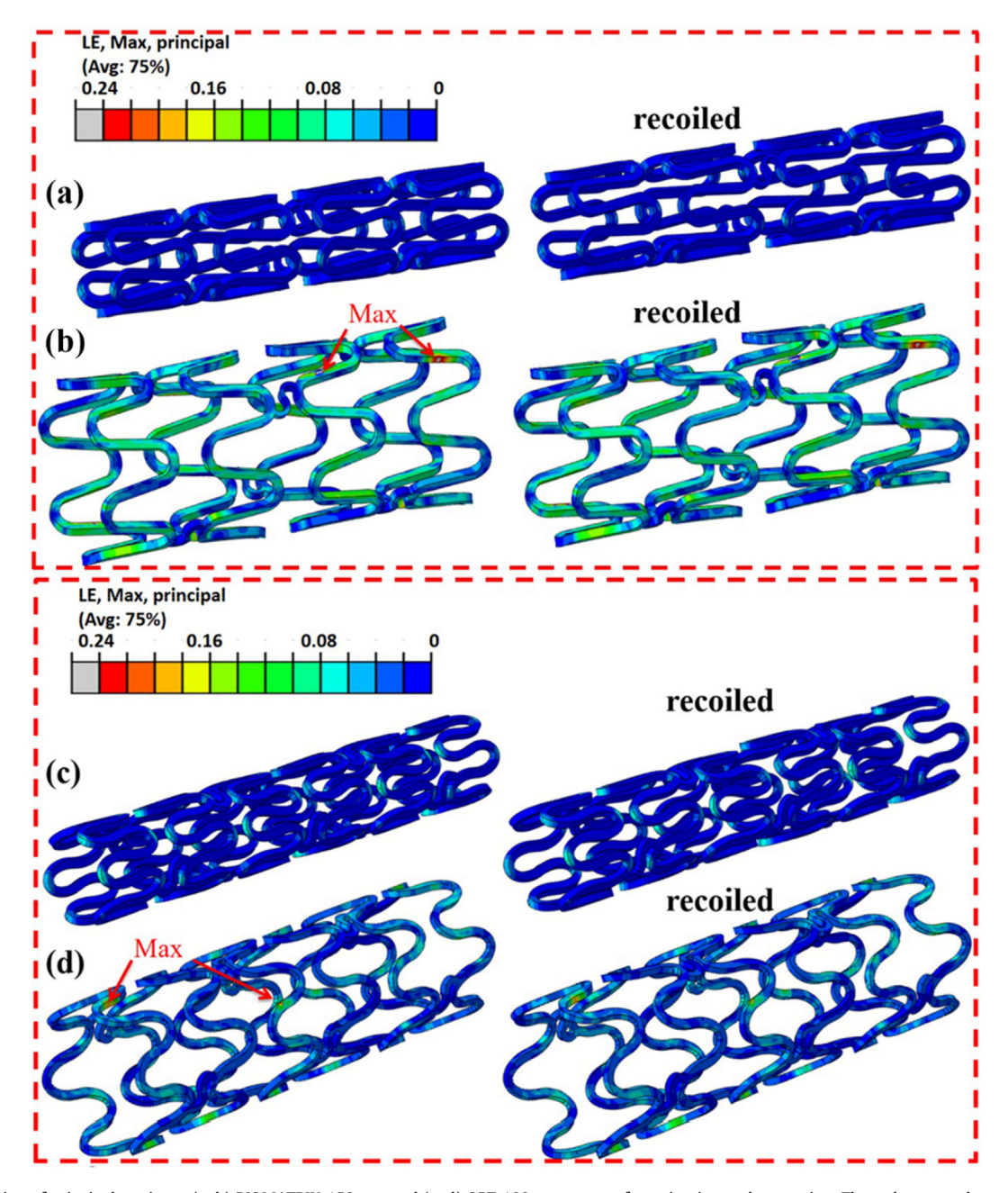


Fig. 5. Distribution of principal strain on (a, b) BIOMATRIX-150- μ m and (c, d) OPT-100- μ m stents after crimping and expansion. The red arrows show the sites with the maximum principal strain.

4.2. Synergy of multiple parameters

To consider the synergy of multiple parameters, the projections of two planes were used to study the law of action. Fig. 10 shows the contour slices of the four objective functions (PEEQ_{expand}, coverage, RS and RR) against the four variables L, R, W1 and W2. Fig. 10a shows that the equivalent plastic strain for expanding PEEQ_{expand} is affected by the L and R of the stent. Appropriately increasing the two values reduces PEEQ_{expand} (upper left corner of Fig. 10a), and reducing the value of W1 can also achieve a similar result (herein, W2 is approximately 0.20 mm; left side of Fig. 10b). For radial strength, the best position is the opposite. The shorter the stent (i.e., the smaller the values of L and L0, the higher the value of RS (left of Fig. 10c). When L1 and L2 are approximately 0.18 and 0.15 mm, respectively, then RS is the largest (right side of Fig. 10d). The minimum value of RR and the maximum value of the

radial strength are consistent. When L is 0 and R is approximately 0.315 mm, the RR of the support is the smallest (left of Fig. 10e). Thus, appropriately increasing the value of W1 can also achieve this result; at this time, the value of W2 is approximately 0.15 mm (right of Fig. 10f). For coverage, W1 is large only when the stent is extremely wide; thus, this point should be considered during optimisation (Fig. 10g and h). The equivalent plastic strain and radial strength are a pair of competing goals. The minimum value of RR and the maximum value of the RS are consistent.

4.3. Thinner stent strut, higher radial strength and lower residual stress

To prevent early loss of radial strength, existing degradable stents, such as ABSORB GT1 and ABSORB BVS, have high thicknesses of 150 and 157 μ m, respectively (Fig. 11) [46–48]. However,

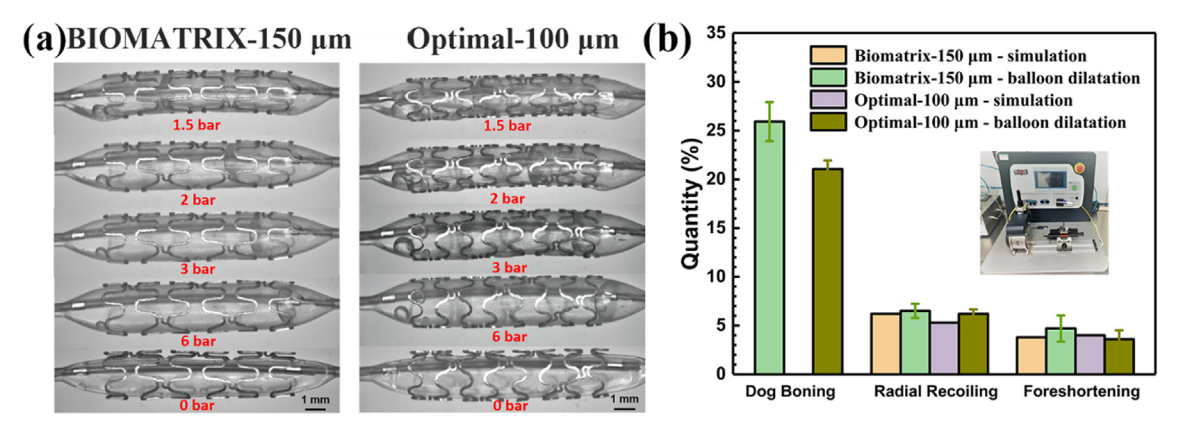


Fig. 6. (a) Balloon expansion experiment of BIOMATRIX-150 μm and OPT-100 μm stents. (b) Dog boning, radial recoiling and foreshortening of BIOMATRIX-150 μm and OPT-100 μm stents. The inserted picture shows the Radial Compression Machine.

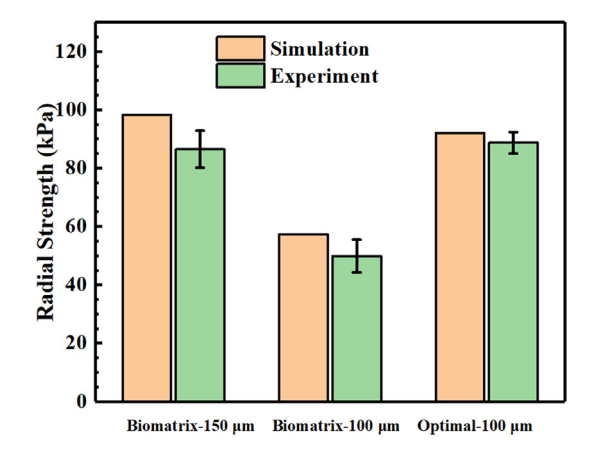


Fig. 7. Radial strengths and their comparison with simulation results for BIOMATRIX-150 μm , BIOMATRIX-100 μm and OPT-100 μm stents.

excessively thick struts affect the stent endothelialisation process and increase the risk of late thrombotic stenosis [49]. Kolandaivelu et al. [16] reported that the risk of thrombosis is increased when the strut thickness exceeds 100 µm (blue dashed line). In addition, the uniformity of stent compression and expansion is a challenge. Micro-cracks and even expansion fractures easily occur if the residual stress after stent deformation is highly concentrated. For example, Zhang et al. [50] designed a BMgS based on the structure of degradable polymer scaffolds and discovered that the corners and links of the stent are prone to strut fracture under high residual stress. Conversely, stress concentrations can be effectively minimised by optimising the equivalent plastic strain of the BMgS; however, this can result in the insufficient supporting capacity of the scaffold or thick struts. The radial strength of the optimised stent reported by Chen et al. [38] is 97 kPa (less than 100 kPa), which only seems acceptable. However, the thickness of their BMgS is 150–160 μ m, which is too large for a stent.

Herein, we found that the above problems can be effectively addressed by structural optimisation design. Compared with the original BIOMATRIX-100- μ m stent, the radial strength of the optimal OPT-100- μ m stent increased by 78.0% (89 kPa vs 50 kPa) and decreased significantly (0.3% vs 0.9%) in the high stress area (\geq 100 MPa). The experimental results of radial strength are less than expected, which can be attributed to the unevenness of the organisation and defects introduced during pipe processing. The wall thickness of the optimal stent is 100 μ m, which is close to the cobalt-chromium alloy stent Xience PrimeTM (81 μ m) [46].

4.4. Perspectives on the future development of thin-walled BMgS structural design

Whether it is permanent or biodegradable stents, the strut thickness is an important parameter. Increased strut thickness is associated with a significant increase in late thrombotic stenosis rate and increased probability of ST-segment elevation myocardial infarction [14-21,27-29]. Both biodegradable polymeric and metallic stents are affected by thick struts (Fig. 10). Thus, the new generation of biodegradable polymeric and metallic stents are developing towards thin struts. However, thin-walled stents can easily lead to insufficient radial strength or stress concentration, but there are ways to improve, such as structural optimisation design. Herein, we propose a structural design of a thin-walled (100-um thick) BMgS. The structure is parameterised and set as four parameters: L, W1, R and W2. Combined with Section 4.2, reducing the L of the stent can effectively increase the radial support strength of the stent. This result may contribute to further optimisation studies for a series of scaffolds.

As one of our optimisation goals, PEEQ is expected to make the BMgS deform uniformly during the crimping and expansion process, which can reduce the high-stress areas and the probability of immediate expansion fractures. In this study, two parameters, the width of the support ring (W1) and the width of the arc (W2), are used to study the structural changes of struts with unequal widths. Combining Fig. 8 (a)–(h), it can be deduced from the parameter changes that the optimised widths were significantly reduced, to decrease the effect of the equivalent plastic strain of the scaffold.

The parameter contrasts of the stents before and after optimization are shown in Table 3. Compared with the BIOMATRIX-100- μm stent, the radial strength of the OPT-100 μm stent has increased by 78.0% (89 kPa vs 50 kPa) and the RR and foreshortening rates of the stent were reduced by 38.6% (6.2% vs 10.1%) and 52.0% (3.6% vs 7.5%), respectively. Compared with the BIOMATRIX-150 μm stent, the PEEQ_{expand} of the OPT-100- μm stent is not much different (0.206 vs 0.193), and the maximum principal strain after dilation is decreased by 26.9% (0.207 vs 0.283) [41]. The thinner stent strut (100 μm vs 150 μm) and smaller surface coverage (16.7% vs 26.7%) of the optimal stent are expected to promote endothelialization and have better biocompatibility.

This study has some limitations. Firstly, the thickness and shape of the parameterised design of the stent were fixed. The design of a more accurate and comprehensive stent structure design optimisation strategy in the future may be the direction of stent development. For example, using free topology optimization to replace parameter optimization may be a direction of future development,

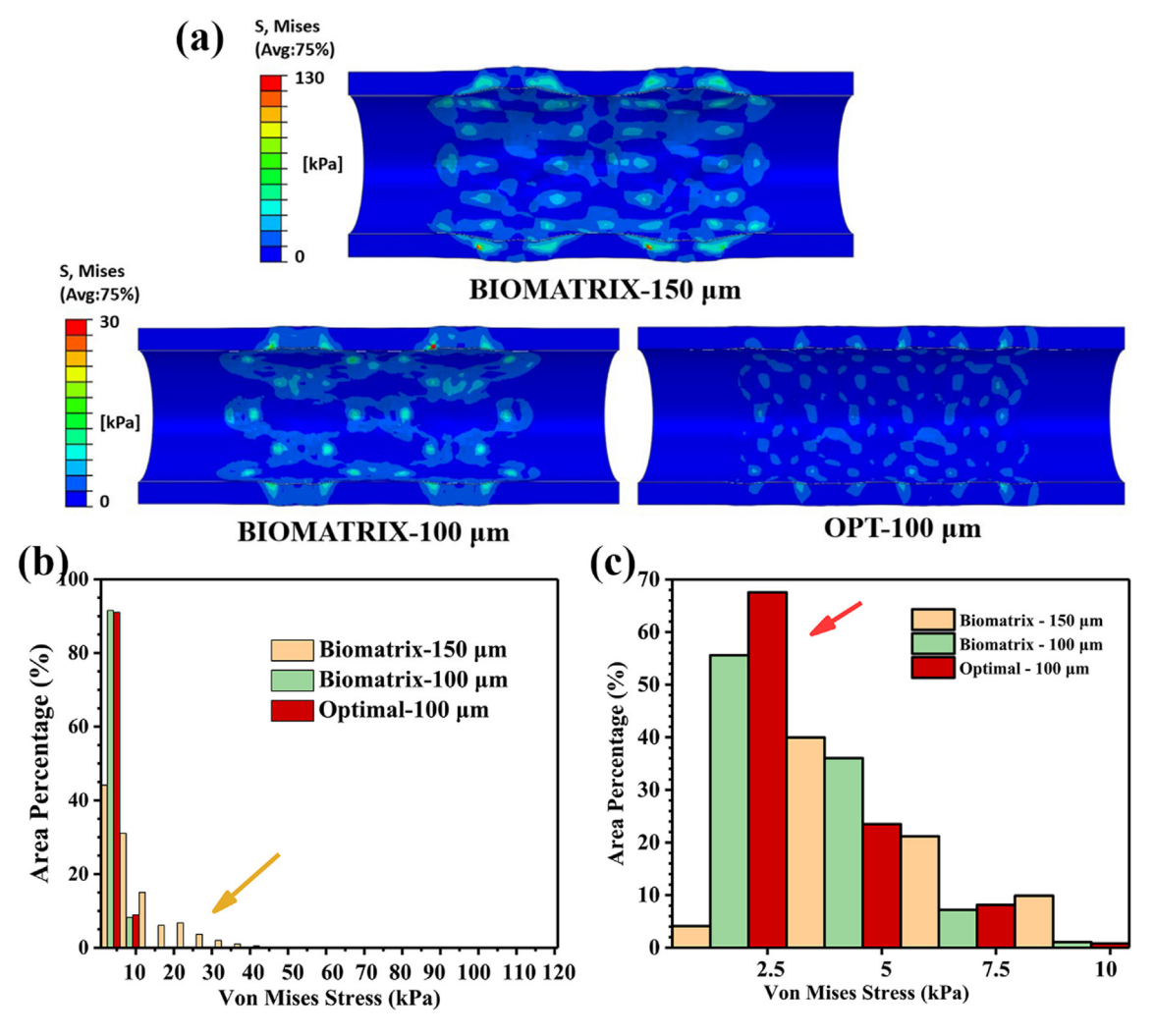


Fig. 8. (a) The von Mises stress distribution of blood vessels after BIOMATRIX-150 μm, BIOMATRIX-100 μm and OPT-100 μm stents implantation. For comparison, the maximum stress on the blood vessels by the 100-μm stent was uniformly set to 30 kPa. (b and c) Histogram of the area distribution of von Mises stress in the blood vessel after stent implantation. The yellow and red arrows indicate the high- and low-stress areas of the blood vessel after stent implantation, respectively.

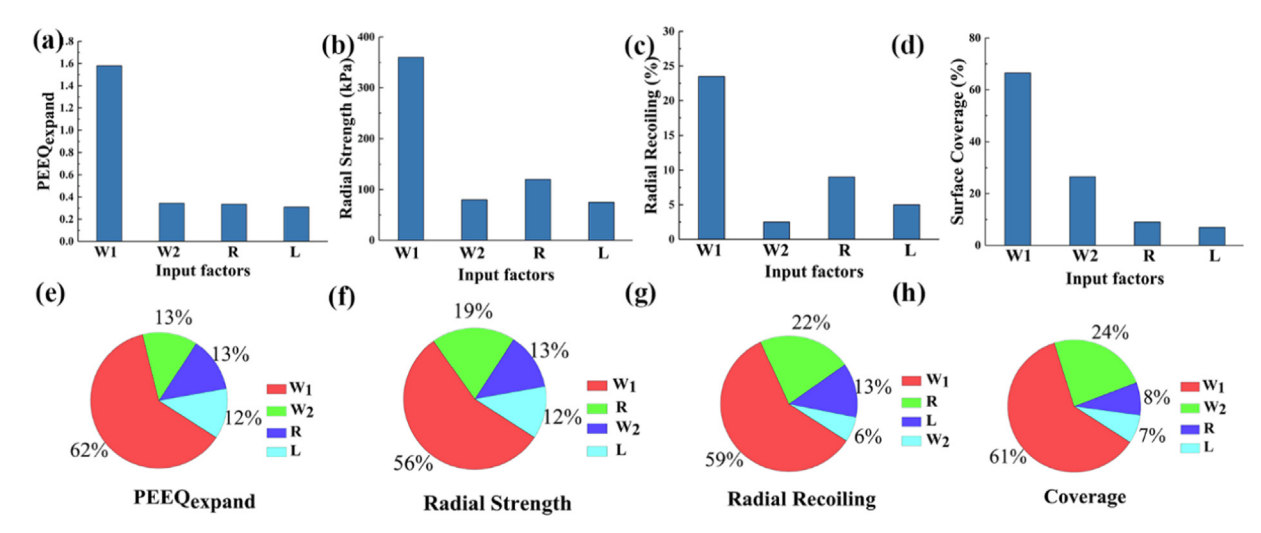


Fig. 9. Range values of (a) PEEQ_{expand}, (b) radial strength, (c) radial recoiling, (d) coverage and normalized at the initial state of four input factors: (e) W1, (f) W2, (g) R and (h)

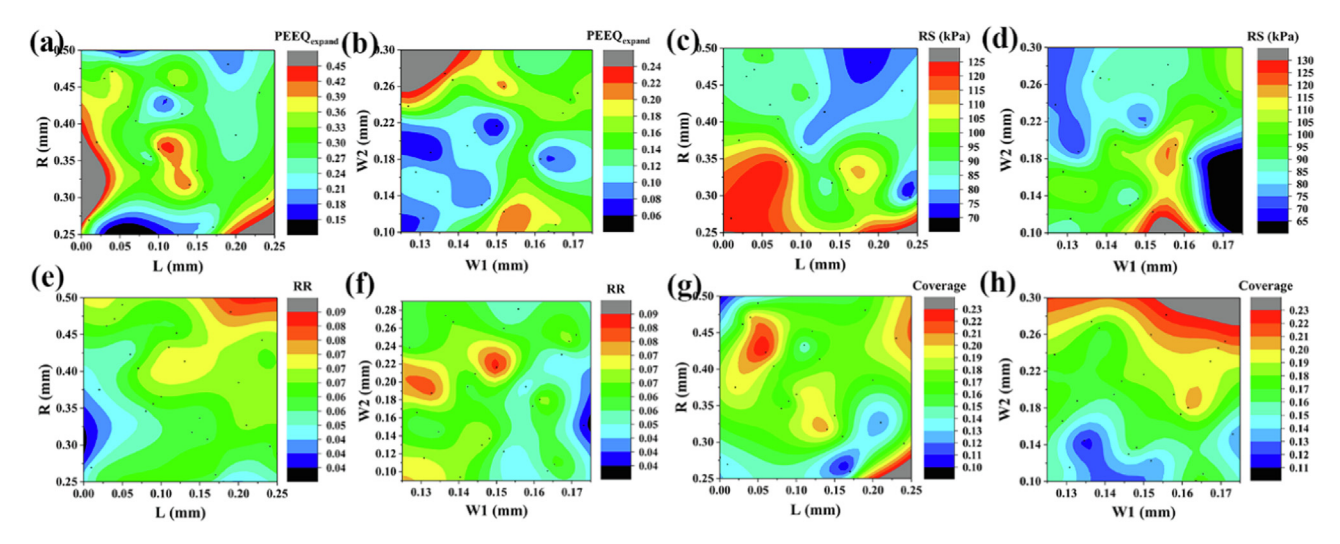


Fig. 10. Four-dimensional response surface projection of the sample points for the BIOMATRIX-100 μm stent platform design in the (a, b, c, d) *L–R* and (e, f, g, h) *W1–W2* planes.

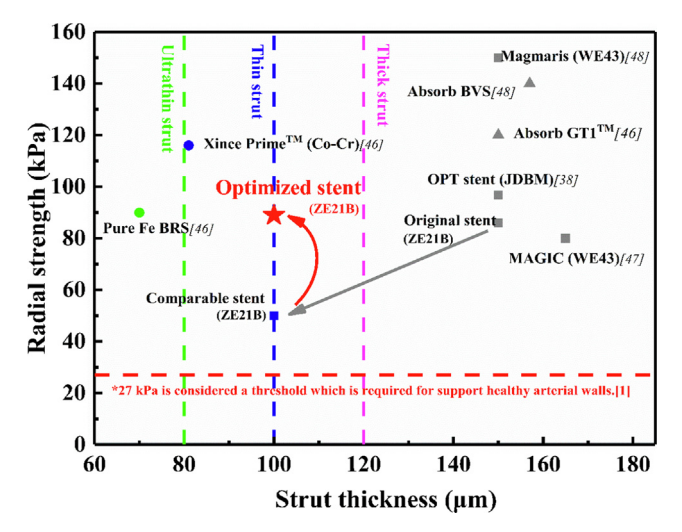


Fig. 11. The effect of stent thickness on radial strength [1,38,46–48]. Stent thickness was defined as ultrathin \leq 80 μ m; thin 81 to 100 μ m; intermediate 101 to 120 μ m; thick \geq 120 μ m. *27 kPa is considered a threshold which is required for support healthy arterial walls [1].

but it would be too expensive and complex from a computational point of view. Secondly, the vessels studied here are based on ideal geometry. Intra-vital imaging and patient-specific arterial geometry would help provide a more instructive output. Finally, this study belongs to prospective research, and the laboratory cannot stably produce matched thin-walled microtubes. In future studies, thinner and more stable quality microtubes will be the guarantee of scaffold product development.

5. Conclusions

In this study, a type of thin-walled biodegradable ZE21B alloy stent structural optimisation design was verified by experiments. RSM proxy model optimisation was employed to obtain the optimal parameters, and multiple properties of the BMgS and its performance were discussed. Based on the results, the following conclusions are drawn.

- 1) Reducing the thickness of a stent can effectively reduce the damage to the blood vessel. Compared with the BIOMATRIX-150-μm stent, the BIOMATRIX-100-μm stent reduced the maximum von Mises stress on the blood vessel by 76.6% (30 kPa vs 128 kPa). Furthermore, for the same thickness, the optimised OPT-100-μm stent is 18 kPa (compared with BIOMATRIX-100-μm stent, which was decreased by 40.0%).
- 2) Compared with the BIOMATRIX-150-µm stent, the maximum principal strain of OPT-100-µm after dilation decreased by 26.9% (0.207 vs 0.283). Histograms of maximum principal stresses show that OPT-100-µm stent significantly increased (58.2% vs 36.8%) in the low-stress area (≤2.5 kPa), and then the stress accounted for a relatively small proportion (0.3% vs 0.9%) in the stress area of 2.5−5 kPa.
- 3) Experimental measurements showed that the radial strength of the OPT-100- μ m stent matched the effect of BIOMATRIX-150- μ m stents (89 ± 4 kPa vs 86 ± 6 kPa). Furthermore, compared with the BIOMATRIX-150- μ m stent, the OPT-100- μ m stent had small RR (6.2% vs 6.5%), foreshortening (3.6% vs 4.7%) and coverage (16.7% vs 26.7%).

Table 3Optimization result of BMgS structure compared to the Original stent and Comparative stent.

Design	Geometry structure size					Radial strength (kPa)	PEEQ _{expand}	Radial recoiling (%)	Fore-shorting (%)	Dog boning (%)	Coverage (%)
	Thickness (mm)	W1 (mm)	W2 (mm)	L (mm)	R (mm)						
Original stent	0.15	0.14	0.14	0.40	0.20	86	0.193	6.5	4.7	25.9	26.7
Comparable stent	0.10	0.14	0.14	0.40	0.20	50	0.151	10.1	7.5	31.7	26.7
Optimal stent	0.10	0.126	0.107	0.007	0.30	89	0.206	6.2	2.6	21.1	16.7

Declaration of Competing Interest

The authors declare that they have no known competing financial interests or personal relationships that could have appeared to influence the work reported in this paper.

Acknowledgements

This work was supported by the National Key Research and Development Program of China (No. 2018YFC1106703) and National Natural Science Foundation of China (No. U1804251).

References

- [1] D. Shen, H. Qi, W. Lin, W. Zhang, D. Bian, X. Shi, L.i. Qin, G. Zhang, W. Fu, K. Dou, B.o. Xu, Z. Yin, J. Rao, M. Alwi, S. Wang, Y. Zheng, D. Zhang, R. Gao, PDLLA-Zn-nitrided Fe bioresorbable scaffold with 53-μm-thick metallic struts and tunable multistage biodegradation function, Sci. Adv. 7 (23) (2021).
- [2] H. Jinnouchi, S. Torii, A. Sakamoto, F.D. Kolodgie, R. Virmani, A.V. Finn, Fully bioresorbable vascular scaffolds: lessons learned and future directions, Nat. Rev. Cardiol. 16 (5) (2019) 286–304, https://doi.org/10.1038/s41569-018-0124-7.
- [3] S.H. Im, Y. Jung, S.H. Kim, Current status and future direction of biodegradable metallic and polymeric vascular scaffolds for next-generation stents, Acta Biomater. 60 (2017) 3–22, https://doi.org/10.1016/j.actbio.2017.07.019.
- [4] J. Fu, Y. Su, Y.X. Qin, Y. Zheng, Y. Wang, D. Zhu, Evolution of metallic cardiovascular stent materials: A comparative study among stainless steel, magnesium and zinc, Biomaterials 230 (2020), https://doi.org/10.1016/j.biomaterials.2019.119641 119641.
- [5] J. Liu, D. Bian, Y. Zheng, X. Chu, Y. Lin, M. Wang, Z. Lin, M. Li, Y. Zhang, S. Guan, Comparative in vitro study on binary Mg-RE (Sc, Y, La, Ce, Pr, Nd, Sm, Eu, Gd, Tb, Dy, Ho, Er, Tm, Yb and Lu) alloy systems, Acta. Biomater. 102 (2020) 508– 528. https://doi.org/10.1016/j.actbio.2019.11.013.
- [6] D. Son, J. Lee, D.J. Lee, R. Ghaffari, S. Yun, S.J. Kim, J.E. Lee, H.R. Cho, S. Yoon, S. Yang, S. Lee, S. Qiao, D. Ling, S. Shin, J.-K. Song, J. Kim, T. Kim, H. Lee, J. Kim, M. Soh, N. Lee, C.S. Hwang, S. Nam, N. Lu, T. Hyeon, S.H. Choi, D.-H. Kim, Bioresorbable Electronic Stent Integrated with Therapeutic Nanoparticles for Endovascular Diseases, ACS Nano. 9 (6) (2015) 5937–5946, https://doi.org/10.1021/acsnano.5b00651.
- [7] H. Yang, C. Wang, C. Liu, H. Chen, Y. Wu, J. Han, Z. Jia, W. Lin, D. Zhang, W. Li, W. Yuan, H. Guo, H. Li, G. Yang, D. Kong, D. Zhu, K. Takashima, L. Ruan, J. Nie, X. Li, Y. Zheng, Evolution of the degradation mechanism of pure zinc stent in the one-year study of rabbit abdominal aorta model, Biomaterials 145 (2017) 92–105, https://doi.org/10.1016/j.biomaterials.2017.08.022.
- [8] T.O. Barkholt, B. Webber, N.R. Holm, J.A. Ormiston, Mechanical properties of the drug-eluting bioresorbable magnesium scaffold compared with polymeric scaffolds and a permanent metallic drug-eluting stent, Catheter. Cardiovasc. Interv. 96 (7) (2020) E674–E682, https://doi.org/10.1002/ccd.28545.
- [9] S. McMahon, N. Bertollo, E.D.O. Cearbhaill, J. Salber, L. Pierucci, P. Duffy, T. Dürig, V. Bi, W. Wang, Bio-resorbable polymer stents: a review of material progress and prospects, Progr. Polym. Sci. 83 (2018) 79–96, https://doi.org/10.1016/j.progpolymsci.2018.05.002.
- [10] T. Hu, C. Yang, S. Lin, Q. Yu, G. Wang, Biodegradable stents for coronary artery disease treatment: Recent advances and future perspectives, Mater. Sci. Eng. C. Mater. Biol. Appl. 91 (2018) 163–178, https://doi.org/10.1016/j. msec.2018.04.100.
- [11] H.Y. Ang, H. Bulluck, P. Wong, S.S. Venkatraman, Y. Huang, N. Foin, Bioresorbable stents: Current and upcoming bioresorbable technologies, Int. J. Cardiol. 228 (2017) 931–939, https://doi.org/10.1016/j.ijcard.2016.11.258.
- [12] M.-H. Kang, K.-H. Cheon, K.-I. Jo, J.-H. Ahn, H.-E. Kim, H.-D. Jung, T.-S. Jang, An asymmetric surface coating strategy for improved corrosion resistance and vascular compatibility of magnesium alloy stents, Mater. Des. 196 (2020) 109182.
- [13] S.G. Ellis, D.J. Kereiakes, D.C. Metzger, R.P. Caputo, D.G. Rizik, P.S. Teirstein, M. R. Litt, A. Kini, A. Kabour, S.O. Marx, J.J. Popma, R. McGreevy, Z. Zhang, C. Simonton, G.W. Stone, Everolimus-eluting bioresorbable scaffolds for coronary artery disease, N. Engl. J. Med. 373 (2015) 1905–1915, https://doi.org/10.1056/NEJMoa1509038.
- [14] S. Buccheri, D. Capodanno, Bioabsorbable stents: only bad news?, Eur Heart J. Suppl. 21 (2019) B28–B30, https://doi.org/10.1093/eurheartj/suz009.
- [15] M. Iantorno, M.J. Lipinski, H.M. Garcia-Garcia, B.J. Forrestal, T. Rogers, D. Gajanana, K.D. Buchanan, R. Torguson, W.S. Weintraub, R. Waksman, Meta-analysis of the impact of strut thickness on outcomes in patients with drug-eluting stents in a coronary artery, Am. J. Cardiol. 122 (10) (2018) 1652–1660, https://doi.org/10.1016/j.amjcard.2018.07.040.
- [16] K. Kolandaivelu, R. Swaminathan, W.J. Gibson, V.B. Kolachalama, K.L. Nguyen-Ehrenreich, V.L. Giddings, L. Coleman, G.K. Wong, E.R. Edelman, Stent thrombogenicity early in high-risk interventional settings is driven by stent design and deployment and protected by polymer-drug coatings, Circulation 123 (2011) 1400–1409, https://doi.org/10.1161/CIRCULATIONAHA.110.003210.

[17] M.J. Lipinski, R.O. Escarcega, N.C. Baker, H.A. Benn, M.A. Gaglia, R. Torguson, R. Waksman, Scaffold thrombosis after percutaneous coronary intervention with ABSORB bioresorbable vascular scaffold: a systematic review and meta-analysis, JACC Cardiovasc. Interv. 9 (1) (2016) 12–24, https://doi.org/10.1016/j.jcin.2015.09.024.

- [18] G.A. Holzapfel, G. Sommer, C.T. Gasser, P. Regitnig, Peter Regitnig, Determination of layer-specific mechanical properties of human coronary arteries with non-atherosclerotic intimal thickening and related constitutive modeling, Am. J. Physiol. Heart. Circ. Physiol. 289 (5) (2005) H2048–H2058.
- [19] P.K.M. Prithipaul, M. Kokkolaras, D. Pasini, Assessment of structural and hemodynamic performance of vascular stents modelled as periodic lattices, Med. Eng. Phys. 57 (2018) 11–18, https://doi.org/10.1016/j. medengphy.2018.04.017.
- [20] A. Kastrati, J. Mehilli, J. Dirschinger, J. Pache, K. Ulm, H. Schühlen, M. Seyfarth, C. Schmitt, R. Blasini, F.J. Neumann, A. Schömig, Restenosis after coronary placement of various stent types, Am. J. Cardiol. 87 (2001) 34–39, https://doi. org/10.1016/S0002-9149(00)01268-6.
- [21] A. Sakamoto, H. Jinnouchi, S. Torii, R. Virmani, A.V. Finn, Understanding the impact of stent and scaffold material and strut design on coronary artery thrombosis from the basic and clinical points of view, Bioengineering 5 (3) (2018), https://doi.org/10.3390/bioengineering5030071.
- [22] W.J. Lin, H.J. Zhang, W.Q. Zhang, H.P. Qi, G. Zhang, J. Qian, X. Li, L. Qin, H.F. Li, X. Wang, H. Qiu, X.L. Shi, W. Zheng, D.Y. Zhang, R.L. Gao, J.D. Ding, *In vivo* degradation and endothelialization of an iron bioresorbable scaffold, Bioactive. Materials. 6 (4) (2021) 1028–1039, https://doi.org/10.1016/j.bioactmat.2020.09.020.
- [23] C. Pan, Y. Han, J. Lu, Structural Design of Vascular Stents: A Review, Micromachines 12 (7) (2021) 770.
- [24] N. Foin, R.D. Lee, R. Torii, J.L. Guitierrez-Chico, A. Mattesini, S. Nijjer, S. Sen, R. Petraco, J.E. Davies, C. Di Mario, M. Joner, R. Virmani, P. Wong, Impact of stent strut design in metallic stents and biodegradable scaffolds, Int. J. Cardiol. 177 (3) (2014) 800–808, https://doi.org/10.1016/j.ijcard.2014.09.143.
- [25] C. Chen, J. Tan, W. Wu, L. Petrini, L. Zhang, Y. Shi, E. Cattarinuzzi, J. Pei, H. Huang, W. Ding, G. Yuan, F. Migliavacca, Modeling and experimental studies of coating delamination of biodegradable magnesium alloy cardiovascular stents, ACS Biomater. Sci. Eng. 4 (2018) 3864–3873, https://doi.org/10.1021/acsbiomaterials.8b00700.
- [26] N. Li, H. Zhang, H. Ouyang, Shape optimization of coronary artery stent based on a parametric model, Finite Elements Anal. Des. 45 (6–7) (2009) 468–475, https://doi.org/10.1016/j.finel.2009.01.001.
- [27] D.E. Kandzari, J.J. Koolen, G. Doros, J.J. Massaro, H.M. Garcia-Garcia, J. Bennett, A. Roguin, E.G. Gharib, D.E. Cutlip, R. Waksman, B.V. Investigators, Ultrathin bioresorbable polymer sirolimus-eluting stents versus thin durable polymer everolimus-eluting stents, J. Am. Coll. Cardiol. 72 (25) (2018) 3287–3297, https://doi.org/10.1016/j.jacc.2018.09.019. PMID: 30257191.
- [28] W. Wu, L. Petrini, D. Gastaldi, T. Villa, M. Vedani, E. Lesma, B. Previtali, F. Migliavacca, Finite element shape optimization for biodegradable magnesium alloy stents, Ann. Biomed. Eng. 38 (9) (2010) 2829–2840, https://doi.org/10.1007/s10439-010-0057-8.
- [29] J.A. Grogan, B.J. O'Brien, S.B. Leen, P.E. McHugh, A corrosion model for bioabsorbable metallic stents, Acta. Biomater. 7 (9) (2011) 3523–3533, https:// doi.org/10.1016/j.actbio.2011.05.032.
- [30] J.L. Li, F. Zheng, X. Qiu, P. Wan, L.L. Tan, K. Yang, Finite element analyses for optimization design of biodegradable magnesium alloy stent, Mat. Sci. Eng. C-Mater. 42 (2014) 705-714, https://doi.org/10.1016/j.msec.2014.05.078.
- [31] S. Tammareddi, G. Sun, Q. Li, Multiobjective robust optimization of coronary stents, Mater. Des. 90 (2016) 682–692, https://doi.org/10.1016/ j.matdes.2015.10.153.
- [32] N.W. Bressloff, Multiobjective design of a biodegradable coronary artery stent, Stud. Mechanobiol. Tissue. Eng. Biomater. 15 (2014) 1–28.
- [33] M. Haude, H. Ince, A. Abizaid, R. Toelg, P.A. Lemos, C. von Birgelen, E.H. Christiansen, W. Wijns, F.J. Neumann, C. Kaiser, E. Eeckhout, S.T. Lim, J. Escaned, H.M. Garcia-Garcia, R. Waksman, Safety and performance of the second-generation drug-eluting absorbable metal scaffold in patients with denovo coronary artery lesions (BIOSOLVE-II): 6 month results of a prospective, multicentre, non-randomised, first-in-man trial, Lancet 387 (10013) (2016) 31–39, https://doi.org/10.1016/S0140-6736(15)00447-X.
- [34] H.M. Garcia-Garciaa, M. Haudeb, K. Kukua, A. Hideo-Kajitaa, H. Incec, A. Abizaidd, R. Tölge, P.A. Lemosf, C. Birgeleng, E.H. Christiansenh, W. Wijnsi, J. Escanedj, J. Dijkstrak, R. Waksmana, *In vivo* serial invasive imaging of the second-generation drug-eluting absorbable metal scaffold (MAGMARIS DREAM-2G) in de novo coronary lesions: insights from the biosolve-ii first-in-man trial, Int. J. Cardiol. 255 (2018) 22–28, https://doi.org/10.1016/j.iicard.2017.12.053.
- [35] M. Haude, H. Ince, S. Kische, A. Abizaid, R. Tölg, P.A. Lemos, N.M. Van Mieghem, S. Verheye, C.V. Birgelen, E.H. Christiansen, Sustained safety and clinical performance of a drug-eluting absorbable metal scaffold up to 24 months: pooled outcomes of BIOSOLVE-II and BIOSOLVE-III, EuroIntervention 13 (4) (2017) 432–439.
- [36] H. Li, X. Wang, Y. Wei, T. Liu, J. Gu, Z. Li, M. Wang, D. Zhao, A. Qiao, Y. Liu, Multi-objective optimizations of biodegradable polymer stent structure and stent microinjection molding process, Polymers 9 (1) (2017) 20, https://doi.org/10.3390/polym9010020.
- [37] C. Chen, J. Chen, W. Wu, Y. Shi, L. Jin, L. Petrini, L. Shen, G. Yuan, W. Ding, J. Ge, E.R. Edelman, F. Migliavacca, *In vivo* and *in vitro* evaluation of a biodegradable magnesium vascular stent designed by shape optimization strategy,

- Biomaterials 221 (2019), https://doi.org/10.1016/j.biomaterials.2019.119414 119414.
- [38] P.J. Wang, F.R. Nezami, M.B. Gorji, F. Berti, L. Petrini, T. Wierzbicki, F. Migliavacca, E.R. Edelman, Effect of working environment and procedural strategies on mechanical performance of bioresorbable vascular scaffolds, Acta Biomater. 82 (2018) 34–43, https://doi.org/10.1016/j.actbio.2018.10.020.
- [39] J. Wang, Y. Zhou, Z. Yang, S. Zhu, L. Wang, S. Guan, Processing and properties of magnesium alloy micro-tubes for biodegradable vascular stents, Mater. Sci. Eng. C-Mater. 90 (2018) 504–513, https://doi.org/ 10.1016/j.msec.2018.05.005.
- [40] W. Li, S. Zhu, Y. Sun, S. Guan, Microstructure and properties of biodegradable Mg–Zn–Y–Nd alloy micro-tubes prepared by an improved method, J. Alloy. Compd. 835 (2020) 155369.
- [41] Y. Li, Y. Wang, Z. Shen, F. Miao, J. Wang, Y. Sun, S. Zhu, Y. Zheng, S. Guan, A biodegradable magnesium alloy vascular stent structure: design, optimisation and evaluation, Acta Biomater. 142 (2022) 402–412, https://doi.org/10.1016/j. actbio.2022.01.045.
- [42] S. Pant, N.W. Bressloff, G. Limbert, Geometry parameterization and multidisciplinary constrained optimization of coronary stents, Biomech. Model. Mechanobiol. 11 (2012) 61–82, https://doi.org/10.1007/s10237-011-0293-3.
- [43] J.A. Grogan, B.J. O'Brien, S.B. Leen, P.E. McHugh, A corrosion model for bioabsorbable metallic stents, Acta. Biomater 7 (9) (2011) 3523–3533, https:// doi.org/10.1016/j.actbio.2011.05.032.
- [44] R.V. Joseph, H. Ying, Orthogonal-Maximin Latin Hypercube Designs, Statistica. Sinica. 18 (1) (2012) 171–186.

- [45] G.E. Box, N.R. Draper, A basis for the selection of a response surface design, J. Am. Stat. Assoc. 54 (287) (1959) 622–654, https://doi.org/10.1080/ 01621459.1959.10501525.
- [46] W. Lin, L. Qin, H. Qi, D. Zhang, G. Zhang, R. Gao, H. Qiu, Y. Xia, P. Cao, X. Wang, W. Zheng, Long-term in vivo corrosion behavior, biocompatibility and bioresorption mechanism of a bioresorbable nitrided iron scaffold, Acta. Biomater. 54 (2017) 454–468, https://doi.org/10.1016/j.actbio.2017.03.020.
- [47] R. Erbel, C. Di Mario, J. Bartunek, J. Bonnier, B. de Bruyne, F.R. Eberli, P. Erne, M. Haude, B. Heublein, M. Horrigan, C. Ilsley, D. Böse, J. Koolen, T.F. Lüscher, N. Weissman, R. Waksman, Temporary scaffolding of coronary arteries with bioabsorbable magnesium stents: a prospective, non-randomised multicentre trial, The Lancet 369 (2007) 1869–1875, https://doi.org/10.1016/S0140-6736 (07)60853-8.
- [48] T.O. Barkholt, B. Webber, N.R. Holm, J.A. Ormiston, Mechanical properties of the drug-eluting bioresorbable magnesium scaffold compared with polymeric scaffolds and a permanent metallic drug-eluting stent, Catheter. Cardio. Inte. (2019) 1–9, https://doi.org/10.1002/ccd.28545.
- [49] D. Bian, X. Zhou, J. Liu, W. Li, D. Shen, Y. Zheng, W. Gu, J. Jiang, M. Li, X. Chu, L. Ma, X. Wang, Y. Zhang, S. Leeflang, J. Zhou, Degradation behaviors and in-vivo biocompatibility of a rare earth-and aluminum-free magnesium-based stent, Acta. Biomater 124 (2021) 382–397, https://doi.org/10.1016/j.actbio.2021.01.031.
- [50] J. Zhang, H. Li, W. Wang, H. Huang, J. Pei, H. Qu, G. Yuan, Y. Li, The degradation and transport mechanism of a Mg-Nd-Zn-Zr stent in rabbit common carotid artery: A 20-month study, Acta Biomater. 69 (2018) 372–384, https://doi.org/ 10.1016/j.actbio.2018.01.018.